

# Spatial control of the conductivity in $SrTiO_3$-based heterointerfaces using inkjet printing

**Hvid-Olsen, T; Gadea, C; Holde, F B; Hoffmann, K M; Jespersen, T S; Grove-Rasmussen, K; Trier, F; Christensen, D V**

*Published in:*
Journal of Physics: Energy

*Link to article, DOI:*
10.1088/2515-7655/ac9084

*Publication date:*
2022

*Document Version*
Publisher's PDF, also known as Version of record

Journal of Physics: Energy

PAPER

# Spatial control of the conductivity in $SrTiO_3$-based heterointerfaces using inkjet printing

T Hvid-Olsen[1], C Gadea[1], F B Holde[1], K M Hoffmann[1], T S Jespersen[1], K Grove-Rasmussen[2], F Trier[1,*] and D V Christensen[1,*]

[1] Department of Energy Conversion and Storage, Technical University of Denmark, 2800 Kgs. Lyngby, Denmark
[2] Center for Quantum Devices, Niels Bohr Institute, University of Copenhagen, 2100 Copenhagen, Denmark
* Authors to whom any correspondence should be addressed.

**E-mail:** fetri@dtu.dk and dechr@dtu.dk

**OPEN ACCESS**

**RECEIVED**
15 June 2022

**REVISED**
25 August 2022

**ACCEPTED FOR PUBLICATION**
8 September 2022

**PUBLISHED**
29 September 2022



**Keywords:** complex oxide heterostructures, inkjet printing, two-dimensional electron gas, spatial confinement, device patterning, $SrTiO_3$, $LaAlO_3$

## Abstract

Interfaces between complex oxides host a plethora of functional properties including enhanced ionic conductivity, gate-tunable superconductivity and exotic magnetic states. The enhanced electronic, ionic and magnetic properties along the oxide interfaces are generally exploited in functional devices by spatial confinement of ions and electrons. Different patterning methods have been used to spatially control the conductivity at the interface, but a key limitation is the multiple steps needed to fabricate functional devices. In this investigation, inkjet printing of thermally stable oxides is introduced as an alternative pathway for spatially controlling the interface conductivity. We inkjet print yttrium-stabilized zirconia and $TiO_2$ with various shapes and use these as physical masks to confine the electronic conductivity in $SrTiO_3$-based heterostructures. By performing *in-situ* transport measurements of the electrical conductivity as $LaAlO_3$ and $\gamma$-$Al_2O_3$ are deposited on $SrTiO_3$, we witness the birth of the interface conductivity and find a consistent transient behavior as conductivity emerges in patterned and non-patterned heterostructures. We find that conductivity appears after the first laser pulse in the pulsed laser deposition corresponding to the film covering only a few percent of the substrate. We attribute the emergence of conductivity to oxygen vacancies formed by a combination of plasma bombardment and oxygen transfer across the interface during growth. In this vein, inkjet patterned hard masks protects the $SrTiO_3$ substrate, effectively confining the conductivity. The study paves a scalable way for realizing energy devices with spatially controlled electronic and ionic interface conductivity.

## 1. Introduction

Oxide interfaces host a variety of interesting properties for energy and information technologies including enhanced ionic transport, gate-tunable superconductivity and exotic magnetic states. The properties of oxide interfaces play a crucial role in developing the next generation of energy-saving electronics based on spintronics or neuromorphic computations [1, 2] as well as achieving high chemical stability and fast ionic conduction in energy materials [3]. A key example is the numerous properties observed at the conducting interface between $LaAlO_3$ and $SrTiO_3$, many of which are absent in the parent materials. Devices based on the $LaAlO_3/SrTiO_3$ heterostructure feature, e.g. electrostatic on/off switching of superconductivity [4], electron pairing without coherent superconductivity [5, 6] and electrically controllable ferromagnetism at room temperature [7].

Two strategies are typically employed when forming devices with spatially confined electronic or ionic conductivity at oxide interfaces: (a) Patterns in resist are defined using, e.g. UV or e-beam lithography and used to spatially control etching, thin film deposition or $Ar^+$-ion irradiation [8–10]. For instance, Trier *et al* used e-beam lithography followed by selective wet chemical etching and pulsed laser deposition (PLD) to produce hall-bar devices with electron mobilities of 8700 $cm^2\ Vs^{-1}$ at 2 K [11]. (b) Local probes such as a

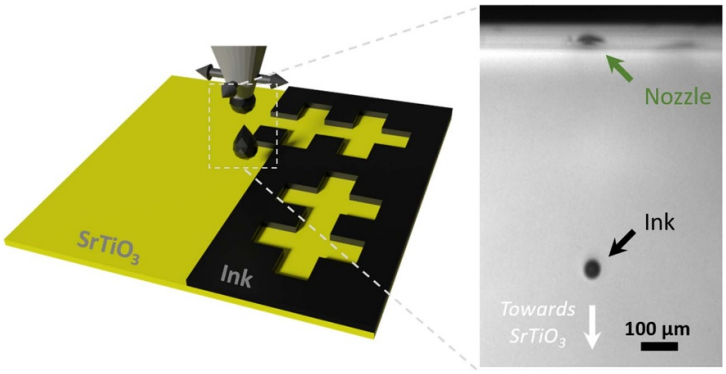


**Figure 1.** Schematic of the inkjet patterning process. The nozzle (grey) moves in the horizontal plane jetting ink onto the substrate below it with spatial selectivity. The inset shows an image of a ink droplet jetted from the nozzle and falling towards the sample surface.

conducting atomic force tip have been successfully used to induce conductivity or insulating regions. For conductive atomic force microscopy, lines of conductivity with a width down to 3 nm have been induced by scanning a positively charged tip on the $LaAlO_3$ or $\gamma$-$Al_2O_3$ surface and reversibly erased using a negative charge [12–14]. In both cases, however, multiple steps are needed. In the case of lithography, after spinning, exposure, baking and development, the patterned resist is incompatible with the typical growth temperatures for oxide films and deposition of a hard mask is generally needed [11, 15, 16]. When using resist to spatially define the removal of material, special care should be taken to avoid modifying the electronic properties of the remaining oxides [10]. C-AFM offers a versatile platform for patterning, but a canvas defined with lithography is needed and the induced conductivity is unstable at room temperature [17] and can only be formed if the initial resistance of the interface is high prior to the c-AFM writing [12, 14].

Inkjet printing has attracted a lot of attention in multiple areas as a versatile, and scalable method for forming patterned structures. The method is fast, automatized, cheap and can be used to coat a large range of materials [18–20]. Inkjet printing is used in diverse areas ranging from biology with printed mammalian cells [21] and SERS substrates for molecular and chemical analysis [22], to energy research where it has been used to fabricate thin-film anodes in battery technology [23] and functional electronic materials [24]. Inkjet printing has also been used to print various oxides including $SrTiO_3$ buffer layers [25], thick $BaTiO_3$ layers [26], as well as $LaNiO_3$ electrodes [27].

Here, we demonstrate how inkjet printing can be used as a fast method to pattern the conductivity at the heterointerfaces formed by depositing either $LaAlO_3$ or $\gamma$-$Al_2O_3$ on $SrTiO_3$. We inkjet print a thermally stable oxide hard mask preventing $LaAlO_3$ or $\gamma$-$Al_2O_3$ to be deposited directly on $SrTiO_3$ in certain areas and use this to confine the metallic conductivity in the areas without inkjet printing. We further investigate the electronic properties in the patterned regions *in-situ* as they emerge during the PLD.

## 2. Inkjet patterning

Inkjet printing, as illustrated in figure 1, was performed by jetting droplets of ink with either dissolved $TiO_2$ or yttrium-stabilized zirconia (YSZ) onto a $SrTiO_3$ substrate in a predefined pattern. The printing is followed by a calcination process to obtain solid oxide structures. By controlling the jetting of the oxide ink spatially, the inkjet printing can produce various geometric structures as visualized in figure 2 with a total printing time on the order of a minute for a $5 \times 5$ mm$^2$ substrate. During the oxide inkjet printing, we used a 21.5 $\mu$m wide printer nozzle to jet $TiO_2$ droplets with a diameter of 35 $\mu$m (see inset in figure 1), which land on the $SrTiO_3$ substrate and form 40 $\mu$m solid dots after calcination. Variation of the nozzle size, the surface tension of the ink and substrate as well as the printer settings can yield different droplet sizes, which determines the resolution of the printed patterns [28]. This represents an optimization process that ultimately could lead to nanometer-sized resolution if carefully perfected. Figure 2(a) depicts these dots formed by jetting single droplets with an inter-droplet distance of 200 $\mu$m. In figure 2(b), $TiO_2$ lines with a width of approximately 30 $\mu$m are printed onto a $SrTiO_3$ substrate by jetting interconnected droplets. The fairly straight lines show the potential for the ink droplets to form well-defined patterns. The result of jetting droplets to form large areas surrounding a Hall-bar shape without ink is shown in figure 2(c). In the case of $TiO_2$, the printed area appear with several white points arising from the ink coalescing into an inhomogeneous, nanostructured layer rather than forming a homogeneous film during the solvent evaporation in the calcination process (see figure 2(d)). These imperfections in the printed layer can be avoided by optimizing the composition of the

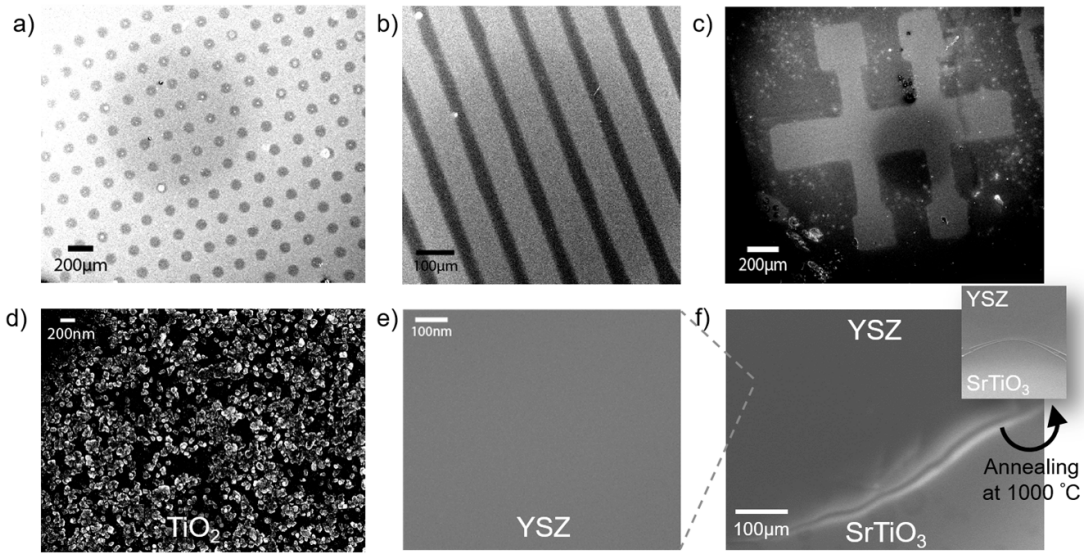


**Figure 2.** Scanning electron micrographs of inkjet printed oxides on a $SrTiO_3$ substrate showing (a) a matrix of $TiO_2$ dots, (b) interconnected dots forming straight lines of $TiO_2$, (c) an ink layer surrounding a hall-bar pattern, (d) high-magnification view of a $TiO_2$ inkjet printed film, (e) high-magnetification view of an YSZ inkjet printed film and (f) the border region of an YSZ inkjet film printed on $SrTiO_3$. The inset shows a border region after annealing at 1000 °C for 1 h in oxygen.

$TiO_2$ ink [28–30] or, as shown in figures 2(e) and (f), by printing YSZ [31]. Here, the YSZ ink forms a homogeneous oxide film without micro- or nanometric cracks.

## 3. Confining conductivity

We further evaluated the capabilities of the ink to spatially confine the interface conductivity in $SrTiO_3$ heterostructures. The oxide ink was first spatially patterned on the $SrTiO_3$ surface such that ink covers the surface except for a region shaped as a hall-bar. The hall-bar was electronically connected with aluminum wires allowing *in-situ* measurements of the transport properties while depositing either $LaAlO_3$ or $\gamma$-$Al_2O_3$ thin films on the patterned substrate at room temperature (see figure 3(a)). The room temperature condition results in the deposition of amorphous $LaAlO_3$ [32], while the $\gamma$-$Al_2O_3$ layer becomes crystalline [33, 34]. For the deposition of $LaAlO_3$ displayed in figure 3(b), the resistance measured on the inkjet patterned Hall-bar is closely matching that observed when depositing directly on an unpatterned $TiO_2$-terminated $SrTiO_3$ substrate. For the $\gamma$-$Al_2O_3$ deposition, the overall trend is similar, but some variations are observed such as the inkjet patterned sample exhibiting a lower resistance of 4.4 kΩ/sq as displayed in figure 3(c). However, by comparing with the results of three nominally identical, unpatterned samples, we attribute the observed discrepancy in figure 3(c) to sample-to-sample variations in $\gamma$-$Al_2O_3/SrTiO_3$. This is consistent with the sample-to-sample variations reported previously for the $\gamma$-$Al_2O_3/SrTiO_3$ heterostructure [33] where the lower carrier density at these interfaces may render more prone to sample-to-sample variations.

In both the patterned and unpatterned cases, the samples are insulating prior to the deposition with a sheet resistance higher than the measurement limit. High resistance is also found below the inkjet printed layer. However, in areas where the $SrTiO_3$ surface is exposed, the resistivity drops several orders of magnitude after the first few laser pulses, corresponding to a $LaAlO_3$ or $\gamma$-$Al_2O_3$ coverage of only a few percent. The resistivity continues to drop after the first few laser pulses until it reaches a stable value on the order of $10^4$ Ω/sq for $LaAlO_3/SrTiO_3$ and, after an upturn, $10^5$ Ω/sq for the $\gamma$-$Al_2O_3/SrTiO_3$. In both cases, the saturated resistance is obtained after deposition of approximately 1 nm oxide layer on $SrTiO_3$. The sudden drop in resistivity after only a few laser pulses is consistent with previous *in-situ* measurements [33], which stands in sharp contrast to *ex-situ* measurements where conductivity is only found above a critical thickness of more than 1 nm at room temperature [32, 35, 36]. Insertion of oxygen into the growth chamber after three laser pulses was previously found to produce insulating $LaAlO_3/SrTiO_3$ interfaces, whereas similar flushing of nitrogen was not degrading the conductivity [33]. Therefore, we link the formation of conductivity to the emergence of oxygen vacancies in $SrTiO_3$, which acts as an electron donor in $SrTiO_3$-based heterostructures as proposed in other studies as well [14, 37–39]. *In-situ* measurements further revealed a different temporal behavior of the conductivity in the case where $LaSr_{1/8}Mn_{7/8}O_3$ was deposited on $SrTiO_3$ under similar deposition conditions [33]. Here, an initial drop of sheet resistance was followed by a large increase into a

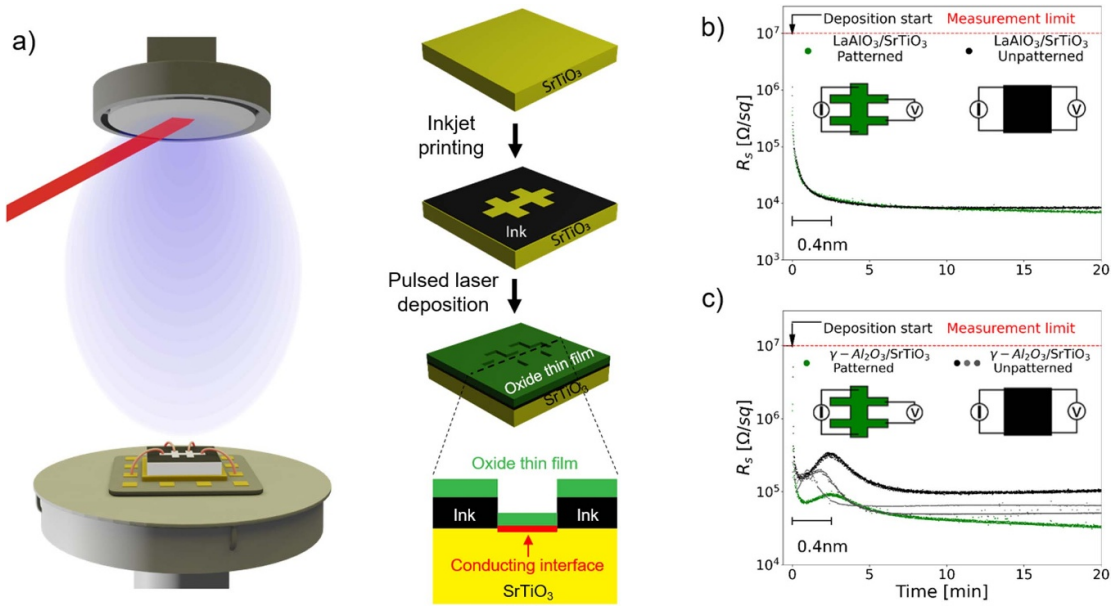


**Figure 3.** (a) Schematic of the *in-situ* measurement setup in the pulsed laser deposition chamber, including an overview of the experimental process for using inkjet printing for confining electronic conductivity in $SrTiO_3$-based heterostructures. *In-situ* sheet resistance measurements of patterned and unpatterned (b) $LaAlO_3/SrTiO_3$ and (c) $\gamma$-$Al_2O_3/SrTiO_3$ heterostructures during pulsed laser deposition. For the $\gamma$-$Al_2O_3/SrTiO_3$ heterostructure, results of three nominally identical unpatterned samples are shown to display the sample-to-sample variation. The insets show the contact setups used for the measurements.

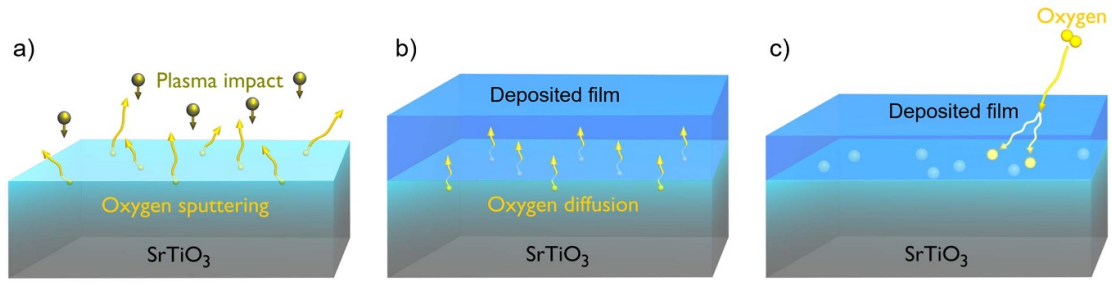


**Figure 4.** Schematic of three processes influencing the final conductivity during the pulsed laser deposition of oxide thin films on $SrTiO_3$: (a) bombardment of the $SrTiO_3$ surface with plasma species to form oxygen vacancies. (b) When thermodynamically favourable, an oxygen deficient deposited film reduces the substrate and generates oxygen vacancies in $SrTiO_3$. (c) Molecular oxygen diffuses to the interface through defects in the deposited film and annihilates the oxygen vacancies in $SrTiO_3$.

highly resistive state after a 30% substrate coverage. The initial drop in resistance when depositing both $LaAlO_3$, $\gamma$-$Al_2O_3$ and $LaSr_{1/8}Mn_{7/8}O_3$ on $SrTiO_3$ is therefore likely a result of the kinetic energy of the bombarding particles that impact the substrate with tens of eV during growth [40] and facilitate removal of oxygen ions from the surface (figure 4(a)). Due to the clear difference in the resulting resistance after depositing $\gamma$-$Al_2O_3$, $LaAlO_3$ and $LaSr_{1/8}Mn_{7/8}O_3$, the composition of the oxide thin film material plays a key role as well. In particular, the high oxygen affinities of the deposited $\gamma$-$Al_2O_3$ and $LaAlO_3$ films facilitate the transfer of oxygen atoms from the $SrTiO_3$ substrate to the oxide thin film in contrast to the low oxygen affinity of $LaSr_{1/8}Mn_{7/8}O_3$ containing multivalent Mn ions that more easily can accommodate oxygen vacancies (figure 4(b)) [32, 41, 42].

The interface conductivity thus appears to be formed from a mixture of bombardment and an interface redox reaction, which are both countered by an oxidation process where oxygen—if present in the environment—fills up oxygen vacancies (figure 4(c)). The oxidation process takes place primarily below the *ex-situ* critical thickness where the $SrTiO_3$ surface is less protected by the thin film, explaining the difference between *ex-situ* and *in-situ* measurements [33]. As apparent from both previous studies [14, 32, 33, 43] as well as the saturation of the electronic properties after deposition of approximately 1 nm (see figure 3), these processes take place close to the $SrTiO_3$ surface. Hence, conductivity is formed on the exposed areas inside the hall-bar as well as on the unpatterned substrate whereas the inkjet printed film acts as a protective layer in regions outside the hall-bar, forming a high-resistive state underneath. Using two-terminal measurements

on devices patterned with $TiO_2$ film, a resistance on the order of 40 MΩ was, however, detected when measuring at room temperature from inside the hall-bar to different places outside the hall-bar. For most purposes, this resistance is negligible compared to the typical two-terminal resistance of 4 kΩ at room temperature measured inside the hall-bar with a comparable distance between the contacts. On the other hand, in the case of the dense YSZ film, the two-terminal resistance was above measurement limit, and we thus attribute the leak resistance in the former case to the inhomogeneous $TiO_2$ film (figure 2(d)), which may form a high-resistive state through a percolating network of conducting lines. The depositions presented here were done at room temperature to simplify the *in-situ* transport measurements, but the YSZ ink also blocks the conductivity and yields insulating interfaces when depositing $\gamma$-$Al_2O_3$ at 650 °C without any measurable leak resistance.

We further tested the thermal stability of the ink by heating a calcinated YSZ film to 1000 °C for 1 h with a ramp rate of 100 °C $h^{-1}$ in an oxygen environment. The ink was thermally stable (see inset in figure 2(f)) and after a subsequent deposition of $\gamma$-$Al_2O_3$ at 650 °C, the two-point resistance was above our measurement limit in regions covered by the annealed YSZ layer. This further supports the usability of the patterning approach in a broad range of temperatures typically used in epitaxial growth of oxide heterostructures.

## 4. Conclusion

Our study introduces inkjet patterning as a viable method for patterning oxide interfaces. It is found to provide a flexible, fast and cheap way to spatially confine conductivity on the micro-scale in $SrTiO_3$-based heterostructures with a thermally stable hard mask approach that does not involve lift-off, etching or several PLDs. Even in the case of an imperfect $TiO_2$ ink that did not result in a fully dense layer after calcination, a high-resistive state was still formed underneath the ink with further potential for realizing 1D quantum physics, study percolating networks or constructing wearable strain sensors from metallic networks formed by a percolating growth template [44, 45]. Advances in stabilizing inkjet inks [28–30], scale-down of characteristic feature sizes as well as the formation of 3D structures through 3D printing further enhances the potential of using the present hard mask approach for forming patterned electronic and ionic conductivity with various 2D and 3D shapes [46, 47]. This allows for inkjet printing to be used for, e.g. control of optoelectronic properties via printing of repetitive conductive patterns, formation of quantum confinement, extraordinary magnetoresistive devices and various ionic or ionotronic devices [3, 48].

## 5. Experimental

$SrTiO_3$ substrates were $TiO_2$-terminated by ultrasonicating for 20 min first in milli-Q water then in acidic solution of 16:1:3 $H_2O$:$HNO_3$:HCl at 70 °C. The substrates were then washed in milli-Q water and annealed for 1 h at 1000 °C with a heating and cooling rate of 100 °C per hour. The $TiO_2$ ink was prepared by mixing titanium(IV) isopropoxide, MDEA, ethanol and water under argon fumes to prevent chemical reactions between the air humidity and the metal precursor as described by Gadea *et al* [28]. The ink was inkjet printed using a Pixdro LP50 printer in various shapes leaving Hall-bars and other patterns exposed. The printed structures were calcined for 1 h at 400 °C in ambient atmosphere. The YSZ ink was made by mixing the precursor zirconium(IV) propoxide mixed with zirconium(III) nitrate hexahydrate dopant, MDEA, water and ethanol as described by Gadea *et al* [31]. After inkjet printing of the YSZ layers, the samples were annealed in ambient atmosphere at a slow ramp rate (15 °C $h^{-1}$) up to 500 °C with 1 h holds at 90 °C, 120 °C and 500 °C to burn off organic material and calcinate the YSZ. Afterward, either amorphous $LaAlO_3$ or crystalline $\gamma$-$Al_2O_3$ thin film oxides were deposited onto the $TiO_2$-terminated $SrTiO_3$ substrates containing either no ink or prepatterned $TiO_2$ or YSZ ink. During the deposition, *in-situ* measurements of the resistance were performed. This was done in a Hall bar geometry for the inkjet patterned samples and using the 4-probe van der Pauw method for the unpatterned substrates. In both cases, the samples were placed in a chip carrier holder with wedge-bonded aluminum wires creating the electrical contact to the sample. The depositions were done using PLD at room temperature at an oxygen background pressure of $3 \times 10^{-6}$ mbar. The ablation of the single-crystalline $LaAlO_3$ and $Al_2O_3$ targets was done with a KrF laser ($\lambda = 248$ nm) using a repetition rate of 0.5 Hz, a laser fluence of 2.5 J $cm^{-2}$ and a fixed target-substrate distance of 40 mm. The samples were analyzed by Zeiss Merlin FEGSEM microscope and a JEOL 7800F SEM.

## Data availability statement

The data that support the findings of this study are available upon reasonable request from the authors.

## Acknowledgments

T H O and F T acknowledge support by research Grant 37338 (SANSIT) from Villum Fonden. D V C and T S J acknowledges support from the Novo Nordic Foundation Challenge Program, Grant No. NNF21OC0066526 (BioMag) and D V C further acknowledges support from the Novo Nordic Foundation Nerd program, Grant No. NNF21OC0068015 (Superior).

## ORCID iDs

T Hvid-Olsen https://orcid.org/0000-0002-8735-1393
K Grove-Rasmussen https://orcid.org/0000-0003-2340-2048
F Trier https://orcid.org/0000-0003-0228-0635
D V Christensen https://orcid.org/0000-0003-0048-7595

## References

[1] Christensen D V *et al* 2022 2022 roadmap on neuromorphic computing and engineering *Neuromorph. Comput. Eng.* **2** 022501
[2] Trier F, Noël P, Kim J V, Attané J P, Vila L and Bibes M 2021 Oxide spin-orbitronics: spin–charge interconversion and topological spin textures *Nat. Rev. Mater.* **7** 1–17
[3] Christensen D V, Chen Y, Esposito V and Pryds N 2019 The role of oxide interfaces in highly confined electronic and ionic conductors *APL Mater.* **7** 013101
[4] Caviglia A D, Gariglio S, Reyren N, Jaccard D, Schneider T, Gabay M, Thiel S, Hammerl G, Mannhart J and Triscone J-M 2008 Electric field control of the $LaAlO_3/SrTiO_3$ interface ground state *Nature* **456** 624–7
[5] Prawiroatmodjo G E D K, Leijnse M, Trier F, Chen Y, Christensen D V, Soosten M V, Pryds N and Jespersen T S 2017 Transport and excitations in a negative-$U$ quantum dot at the $LaAlO_3/SrTiO_3$ interface *Nat. Commun.* **8** 395
[6] Cheng G *et al* 2015 Electron pairing without superconductivity *Nature* **521** 196–9
[7] Bi F, Huang M, Ryu S, Lee H, Bark C-W, Eom C-B, Irvin P and Levy J 2014 Room-temperature electronically-controlled ferromagnetism at the $LaAlO_3/SrTiO_3$ interface *Nat. Commun.* **5** 5019
[8] Chen Y 2015 Nanofabrication by electron beam lithography and its applications: a review *Microelectron. Eng.* **135** 57–72
[9] Stornaiuolo D, Gariglio S, Couto N J G, Fête A, Caviglia A D, Seyfarth G, Jaccard D, Morpurgo A F and Triscone J-M 2012 In-plane electronic confinement in superconducting $LaAlO_3/SrTiO_3$ nanostructures *Appl. Phys. Lett.* **101** 222601
[10] Aurino P P, Kalabukhov A, Tuzla N, Olsson E, Claeson T and Winkler D 2013 Nano-patterning of the electron gas at the $LaAlO_3/SrTiO_3$ interface using low-energy ion beam irradiation *Appl. Phys. Lett.* **102** 201610
[11] Trier F, Prawiroatmodjo G E D K, von Soosten M, Christensen D V, Jespersen T S, Chen Y Z and Pryds N 2015 Patterning of high mobility electron gases at complex oxide interfaces *Appl. Phys. Lett.* **107** 191604
[12] Cen C, Thiel S, Hammerl G, Schneider C W, Andersen K E, Hellberg C S, Mannhart J and Levy J 2008 Nanoscale control of an interfacial metal-insulator transition at room temperature *Nat. Mater.* **7** 298–302
[13] Cheng C, Stefan T, Jochen M and Jeremy L 2009 Oxide nanoelectronics on demand *Science* **323** 1026–30
[14] Christensen D V, von Soosten M, Trier F, Jespersen T S, Smith A, Chen Y and Pryds N 2017 Controlling the carrier density of $SrTiO_3$-based heterostructures with annealing *Adv. Electron. Mater.* **3** 1700026
[15] Banerjee N, Koster G and Rijnders G 2013 Submicron patterning of epitaxial $PbZr_{0.52}Ti_{0.48}O_3$ heterostructures *Appl. Phys. Lett.* **102** 142909
[16] Niu W, Gan Y, Zhang Y, Christensen D V, von Soosten M, Wang X, Xu Y, Zhang R, Pryds N and Chen Y 2017 Suppressed carrier density for the patterned high mobility two-dimensional electron gas at $\gamma$-$Al_2O_3/SrTiO_3$ heterointerfaces *Appl. Phys. Lett.* **111** 021602
[17] Bi F, Bogorin D F, Cen C, Bark C W, Park J-W, Eom C-B and Levy J 2010 "Water-cycle" mechanism for writing and erasing nanostructures at the $LaAlO_3/SrTiO_3$ interface *Appl. Phys. Lett.* **97** 173110
[18] Chung S, Cho K and Lee T 2019 Recent progress in inkjet-printed thin-film transistors *Adv. Sci.* **6** 1801445
[19] Nayak L, Mohanty S, Nayak S K and Ramadoss A 2019 A review on inkjet printing of nanoparticle inks for flexible electronics *J. Mater. Chem.* C **7** 8771–95
[20] Li X, Liu B, Pei B, Chen J, Zhou D, Peng J, Zhang X, Jia W and Xu T 2020 Inkjet bioprinting of biomaterials *Chem. Rev.* **120** 10793–833
[21] Xu T, Jin J, Gregory C, Hickman J J and Boland T 2005 Inkjet printing of viable mammalian cells *Biomaterials* **26** 93–99
[22] Yu W W and White I M 2010 Inkjet printed surface enhanced raman spectroscopy array on cellulose paper *Anal. Chem.* **82** 9626–30
[23] Lawes S, Sun Q, Lushington A, Xiao B, Liu Y and Sun X 2017 Inkjet-printed silicon as high performance anodes for Li-ion batteries *Nano Energy* **36** 313–21
[24] Sirringhaus H, Kawase T, Friend R H, Shimoda T, Inbasekaran M, Wu W and Woo E P 2000 High-resolution inkjet printing of all-polymer transistor circuits *Science* **290** 2123–6
[25] Pollefeyt G, Clerick S, Vermeir P, Feys J, Hühne R, Lommens P and Driessche I V 2014 Ink-jet printing of $SrTiO_3$ buffer layers from aqueous solutions *Supercond. Sci. Technol.* **27** 095007
[26] Tseng W J, Lin S-Y and Wang S-R 2006 Particulate dispersion and freeform fabrication of $BaTiO_3$ thick films via direct inkjet printing *J. Electroceramics* **16** 537–40
[27] Matavž A, Kovač J, Čekada M, Malič B and Bobnar V 2018 Enhanced electrical response in ferroelectric thin film capacitors with inkjet-printed $LaNiO_3$ electrodes *Appl. Phys. Lett.* **113** 012904
[28] Gadea C, Marani D and Esposito V 2017 Nucleophilic stabilization of water-based reactive ink for titania-based thin film inkjet printing *J. Phys. Chem. Solids* **101** 10–17
[29] Padrón-Hernández W Y, Ceballos-Chuc M C, Pourjafari D, Oskam G, Tinoco J C, Martínez-López A G and Rodríguez-Gattorno G 2018 Stable inks for inkjet printing of $TiO_2$ thin films *Mater. Sci. Semicond. Process.* **81** 75–81
[30] Barreiro A M, Pinheiro G K, Wesling B N, Müller D, Scarabelot L T, de Souza L V, Hotza D and Rambo C R 2020 Aerogel-based $TiO_2$ stable inks for direct inkjet printing of nanostructured layers *Adv. Mater. Sci. Eng.* **2020** 4273097

[31] Gadea C, Hanniet Q, Lesch A, Marani D, Jensen S H and Esposito V 2017 Aqueous metal–organic solutions for YSZ thin film inkjet deposition *J. Mater. Chem.* C **5** 6021–9
[32] Chen Y, Pryds N, Kleibeuker J E, Koster G, Sun J, Stamate E, Shen B, Rijnders G and Linderoth S 2011 Metallic and insulating interfaces of amorphous $SrTiO_3$-based oxide heterostructures *Nano Lett.* **11** 3774–8
[33] von Soosten M, Christensen D V, Eom C-B, Jespersen T S, Chen Y and Pryds N 2019 On the emergence of conductivity at $SrTiO_3$-based oxide interfaces—an *in-situ* study *Sci. Rep.* **9** 18005
[34] Chen Y Z, Bovet N, Kasama T, Gao W W, Yazdi S, Ma C, Pryds N and Linderoth S 2014 Room temperature formation of high-mobility two-dimensional electron gases at crystalline complex oxide interfaces *Adv. Mater.* **26** 1462–7
[35] Christensen D V, Trier F, Chen Y Z, Smith A, Nygård J and Pryds N 2013 Controlling interfacial states in amorphous/crystalline $LaAlO_3/SrTiO_3$ heterostructures by electric fields *Appl. Phys. Lett.* **102** 021602
[36] Christensen D V, Trier F, von Soosten M, Prawiroatmodjo G E D K, Jespersen T S, Chen Y Z and Pryds N 2016 Electric field control of the $\gamma$-$Al_2O_3/SrTiO_3$ interface conductivity at room temperature *Appl. Phys. Lett.* **109** 021602
[37] Kalabukhov A, Gunnarsson R, Börjesson J, Olsson E, Claeson T and Winkler D 2007 Effect of oxygen vacancies in the $SrTiO_3$ substrate on the electrical properties of the $LaAlO_3/SrTiO_3$ interface *Phys. Rev.* B **75** 121404
[38] Gunkel F, Hoffmann-Eifert S, Heinen R A, Christensen D V, Chen Y Z, Pryds N, Waser R and Dittmann R 2017 Thermodynamic ground states of complex oxide heterointerfaces *ACS Appl. Mater. Interfaces* **9** 1086–92
[39] Gunkel F, Christensen D V, Chen Y and Pryds N 2020 Oxygen vacancies: the (in)visible friend of oxide electronics *Appl. Phys. Lett.* **116** 120505
[40] Sambri A, Cristensen D V, Trier F, Chen Y Z, Amoruso S, Pryds N, Bruzzese R and Wang X 2012 Plasma plume effects on the conductivity of amorphous-$LaAlO_3/SrTiO_3$ interfaces grown by pulsed laser deposition in $O_2$ and Ar *Appl. Phys. Lett.* **100** 231605
[41] Fu Q and Wagner T 2007 Interaction of nanostructured metal overlayers with oxide surfaces *Surf. Sci. Rep.* **62** 431–98
[42] Fu Q and Wagner T 2005 Metal/oxide interfacial reactions: oxidation of metals on $SrTiO_3$ (100) and $TiO_2$ (110) *J. Phys. Chem.* B **109** 11697–705
[43] Trier F, Christensen D, Chen Y, Smith A, Andersen M and Pryds N 2013 Degradation of the interfacial conductivity in $LaAlO_3/SrTiO_3$ heterostructures during storage at controlled environments *Solid State Ion.* **230** 12–15
[44] Amjadi M, Pichitpajongkit A, Lee S, Ryu S and Park I 2014 Highly stretchable and sensitive strain sensor based on silver nanowire-elastomer nanocomposite *ACS Nano* **8** 5154–63
[45] Gupta R, Kumar A, Sadasivam S, Walia S, Kulkarni G U, Fisher T S and Marconnet A 2017 Microscopic evaluation of electrical and thermal conduction in random metal wire networks *ACS Appl. Mater. Interfaces* **9** 13703–12
[46] Briane M and Milton G W 2009 Homogenization of the three-dimensional Hall effect and change of sign of the Hall coefficient *Arch. Ration. Mech. Anal.* **193** 715–36
[47] Kern C, Kadic M and Wegener M 2017 Experimental evidence for sign reversal of the Hall coefficient in three-dimensional metamaterials *Phys. Rev. Lett.* **118** 16601
[48] Solin S, Thio T, Hines D and Heremans J 2000 Enhanced room-temperature geometric magnetoresistance in inhomogeneous narrow-gap semiconductors *Science* **289** 1530–2